Astronomy & Astrophysics manuscript no. output
May 19, 2025

Large databases of metal-poor stars corrected for 3D and/or NLTE effects

I. Koutsouridou*[1], Á. Skúladóttir[1], and S. Salvadori[1]

Dipartimento di Fisica e Astronomia, Universitá degli Studi di Firenze, Via G. Sansone 1, I-50019 Sesto Fiorentino, Italy.

ABSTRACT

Early chemical enrichment processes can be unveiled by the careful study of metal-poor stars. In our Local Group, we can obtain spectra of individual stars to measure their precise, but not always accurate, chemical abundances. Unfortunately, stellar abundances are typically estimated under the simplistic assumption of local thermodynamic equilibrium (LTE). This can systematically alter both the abundance patterns of individual stars and the global trends of chemical enrichment. The SAGA database compiles the largest catalogue of metal-poor stars in the Milky Way. For the first time, we provide the community with the SAGA catalogue fully corrected for non-LTE (NLTE) effects, using state-of-the-art publicly available grids. In addition, we present an easy-to-use online tool `NLiTE` that quickly provides NLTE corrections for large stellar samples. For further scientific exploration, `NLiTE` facilitates the comparison of different NLTE grids to investigate their intrinsic uncertainties. Finally, we compare the NLTE-SAGA catalogue with our cosmological galaxy formation and chemical evolution model, `NEFERTITI`. By accounting for NLTE effects, we can solve the long-standing discrepancy between models and observations in the abundance ratio of [C/Fe], which is the best tracer of the first stellar populations. At low [Fe/H] < -3.5, models were unable to reproduce the high measured [C/Fe] in LTE, which are lowered in NLTE, aligning with the simulations. Other elements are a mixed bag, where some show improved agreement with the models (e.g. Na) and others appear even worse (e.g. Co). Few elemental ratios do not change significantly (e.g. [Mg/Fe], [Ca/Fe]). Properly accounting for NLTE effects is fundamental for correctly interpreting the chemical abundances of metal-poor stars. Our new `NLiTE` tool, thus, enables a meaningful comparison of stellar samples with chemical and stellar evolution models as well as with low-metallicity gaseous environments at higher redshift.

Key words. Galaxy: abundances - stars: abundances - stars: atmospheres - stars: Population II - line: formation

* e-mail: `ioanna.koutsouridou@unifi.it`

Appendix A: Adopted NLTE grids

Table A.1 lists the NLTE grids that we have adopted from the literature for each chemical species.

Appendix B: Comparison of NLTE corrections

Figures B.1-B.14 show a comparison of different grids of calculated NLTE corrections for different [Fe/H], $T_{\rm eff}$, and log g. The details for each element are discussed in Sec. 2.

Appendix C: The applied corrections

For completeness, we present here discussion of the applied corrections for the NLTE-SAGA database for elements which were not included in Sec. 4.2. The results are shown in Figs. C.1-C.7, for Li, Si, K, Ca, Zn, Sr, and Ba. In all cases, the fiducial $[Fe/H]_{\rm 1D\,NLTE}$ is adopted, i.e. using the mean corrections of Mashonkina et al. (2011) and Bergemann et al. (2012b), see Table A.1.

The left and right panels of Fig. C.1 illustrate the NLTE corrections for A(Li) based on the 3D and 1D grids from Wang et al. (2021) and Lind et al. (2009), respectively. In both cases, the corrections remain above −0.1 dex, except for a handful of stars with high A(Li) > 2.28. The corrections of Lind et al. (2009), reaching close to +0.3 dex, show a clear dependence on log g at fixed metallicity. In contrast, the corrections of Wang et al. (2021), always remaining below +0.1 dex, have no significant correlation with log g but instead show an increasing trend with decreasing $[Fe/H]_{\rm LTE}$. For the same stars the largest difference between the two sets reaches 0.24 dex. We note that when using the limited grid of Sbordone et al. (2010) instead (see Table A.1), we find weak corrections that range from −0.01 to +0.04 dex, and from +0.02 to +0.055 dex for the 1D and 3D cases, respectively.

The net [Si/Fe] corrections (Fig. C.2; left panel) are negative for the majority (∼ 70%) of stars, showing an increasing trend (in absolute values) with decreasing [Fe/H], especially at low log g < 3. However, at [Fe/H] < −2 and high log g > 3, the [Si/Fe] corrections rise up to +0.7 dex, as the Si corrections of Amarsi & Asplund (2017) increase significantly with increasing $T_{\rm eff}$ (see Fig. B.3). Contrarily, the Bergemann et al. (2013) corrections for Si, being small at all $T_{\rm eff}$ and log g values, result in negative net [Si/Fe] corrections for more than 99% of the stars (Fig. C.2; right panel). The average absolute difference between the two correction sets is 0.075 dex, with the largest discrepancy reaching 0.87 dex.

The net corrections for [K/Fe] for all SAGA entries with potassium measurements are negative (Fig. C.3; left panel). The K corrections increase strongly (in absolute magnitude) with increasing metallicity (see Fig. B.5). However, the net corrections show a downturn at $[Fe/H] \lesssim -2.5$, driven by the $\Delta[Fe/H]_{\rm 1D\,NLTE}$ dependence on $[Fe/H]_{\rm LTE}$ (See Fig. 10). When using the Takeda et al. (2002) grid instead of our fiducial grid from Reggiani et al. (2019), the corrections remain largely consistent, differing by < 0.1 dex.

Both the Ca and Fe corrections exhibit a clear dependence on log g. However, some of this effect cancels out and this trend is less pronounced in the net [Ca/Fe] corrections (Fig. C.4). While most Ca corrections are positive (similar to Fe, see Fig. 10), the net [Ca/Fe] corrections vary between −0.2 and +0.1 dex. Using the Spite et al. (2012) grid, instead of our default from Mashonkina et al. (2007), yields very similar results, with a maximum difference of less than 0.12 dex between the two grids.

Fig. C.5 displays the net corrections for [Zn I/Fe] and [Eu II/Fe]. The corrections for Zn I are always positive, increasing with decreasing metallicity down to [Fe/H] ≈ −2, and then leveling off at lower metallicities. Due to the anticorrelation between $\Delta[Fe/H]_{\rm NLTE}$ and $[Fe/H]_{\rm LTE}$ (see Fig. 10), the net corrections of [Zn/Fe] peak around [Fe/H] ≈ −2 and turn negative at $[Fe/H] \lesssim -2.5$. Still, the absolute corrections for [Zn/Fe] remain small, always ≲ 0.1 dex. The corrections for [Eu II/Fe], only available for giant stars, are modest (−0.10 dex < ΔNLTE < 0.15 dex), and show an increasing trend with decreasing log g.

The net [Sr II/Fe] corrections from Mashonkina et al. (2022) lie in the range −0.45 to +0.25 dex and show no clear trend with log g due to their dependence on both $[Fe/H]_{\rm LTE}$ and $[Sr\,II/Fe]_{\rm LTE}$ (Fig. C.6). When using the Bergemann et al. (2012a) grid we find somewhat weaker corrections, with differences up to 0.2 dex (0.06 dex on average).

Finally, in Fig. C.7, we show $\Delta[Ba\,II/H]_{\rm NLTE}$ based on our fiducial 1D NLTE corrections of Mashonkina & Belyaev (2019; top-left), and those of Korotin et al. (2015; top-right); as well as the 1D and 3D NLTE corrections of Gallagher et al. (2020; bottom panels). We do not plot the net [Ba II/Fe] corrections here, to facilitate comparison, as 3D-NLTE corrections for Fe are only available for hot dwarf stars (see Table A.1). All 1D NLTE corrections for Ba exhibit an increasing trend with log g, though the Mashonkina & Belyaev (2019) and Korotin et al. (2015) corrections are on average 0.04 and 0.06 dex higher, respectively, than those of Gallagher et al. (2020) in the overlapping regions. In fact, more than 85% of stars have corrections that differ less than 0.1 dex among the three sets. The observed trend, however, reverses when we consider the 3D corrections of Gallagher et al. (2020); here, stars with higher log g exhibit more negative corrections. In all cases, the corrections span a range of approximately −0.4 to +0.3 dex.

Appendix D: Comparison with NEFERTITI

In the following, we will discuss the comparison of the NLTE-SAGA database with our NEFERTITI model for elements not included in Sec. 5. The results are given in Figs. D.1-D.4 for O, Si, K, Ti, Co, Cu, and Zn. The heavy elements Sr and Ba are currently outside the scope of the model.

Fig. D.1 presents the [O/Fe]–[Fe/H] distribution of inner-halo stars in our NEFERTITI model, in comparison to all SAGA stars with measured O I abundances. We find that the observed and predicted distributions are overall in good agreement. Most of the observed stars have been published with O I abundances already corrected for NLTE effects, e.g. stars from Roederer et al. (2014) who used the O I NLTE corrections of Fabbian et al. (2009); Gratton et al. (2000) who used the prescription by Gratton et al. (1999); Fulbright & Johnson (2003) who used the corrections of Takeda et al. (2000); and others. The net [O I/Fe] NLTE corrections for the rest of the stars are strongest at $[Fe/H]_{\rm LTE} < -2$, reaching ∼ −0.45 dex. In this [Fe/H] range, the O I abundances of ∼ 45% of the stars are reported as upper limits. At [Fe/H] > −2 the corrections for [O I/Fe] are smaller, in the range −0.2 to 0 dex (with the exception of two stars with high [O/Fe] > +1).

Fig. D.2 shows that the $[Si/Fe]_{\rm LTE}$ ratios from SAGA exhibit an increasing trend with decreasing log g at fixed metallicity. This trend disappears after correcting for NLTE effects. The overall distribution becomes flatter, more in agreement with other α-elements such as Mg and Ca (see Fig. 23). Furthermore, after applying the NLTE corrections, the scatter in [Si/Fe] decreases from $\sigma_{\rm LTE} = 0.26$ to $\sigma_{\rm NLTE} = 0.22$, see Fig. D.2.

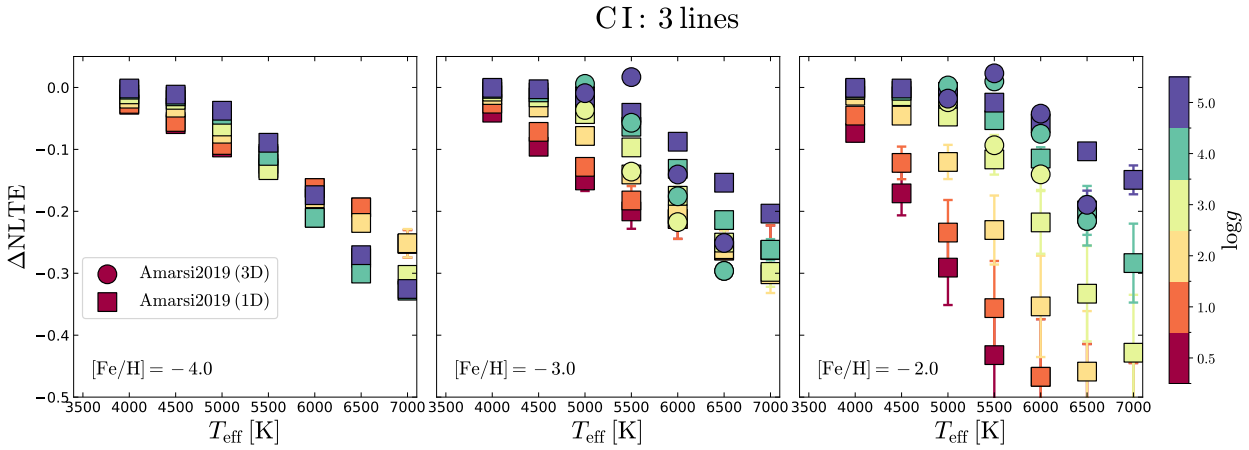

Fig. B.1: Comparison of 1D NLTE (squares) and 3D NLTE (circles) corrections for C I from Amarsi et al. (2019), color-coded by $\log g$. Three metallicities are shown, assuming [C/Fe] = +0.5 in all cases: [Fe/H] = −4 (left), [Fe/H] = −3 (middle), and [Fe/H] = −2 (right). Error bars show the standard deviation between the lines used.

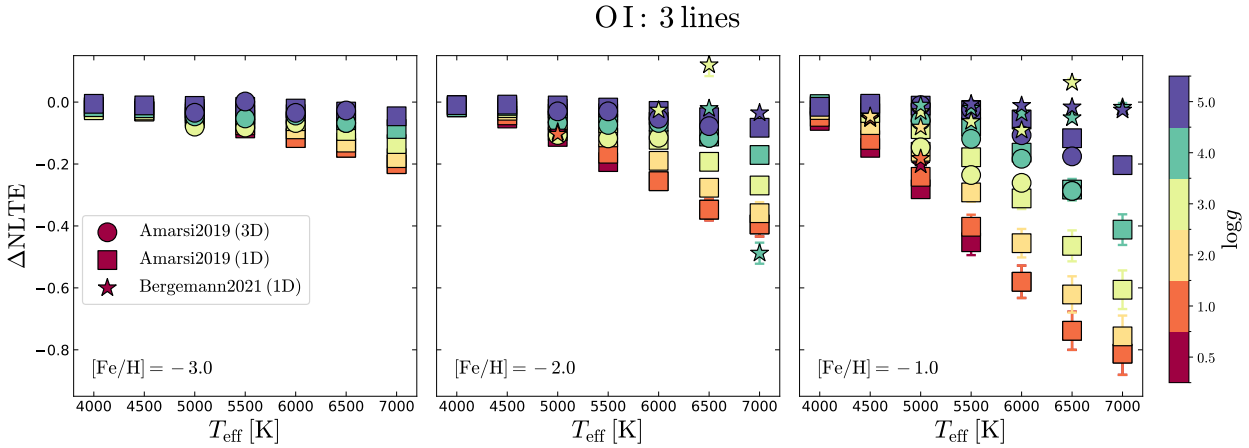

Fig. B.2: Same as Fig. B.1 for O I, assuming [O/Fe] = +0.5, for [Fe/H] = −3, −2, and −1, from left to right. Star symbols show 1D NLTE corrections by Bergemann et al. (2021).

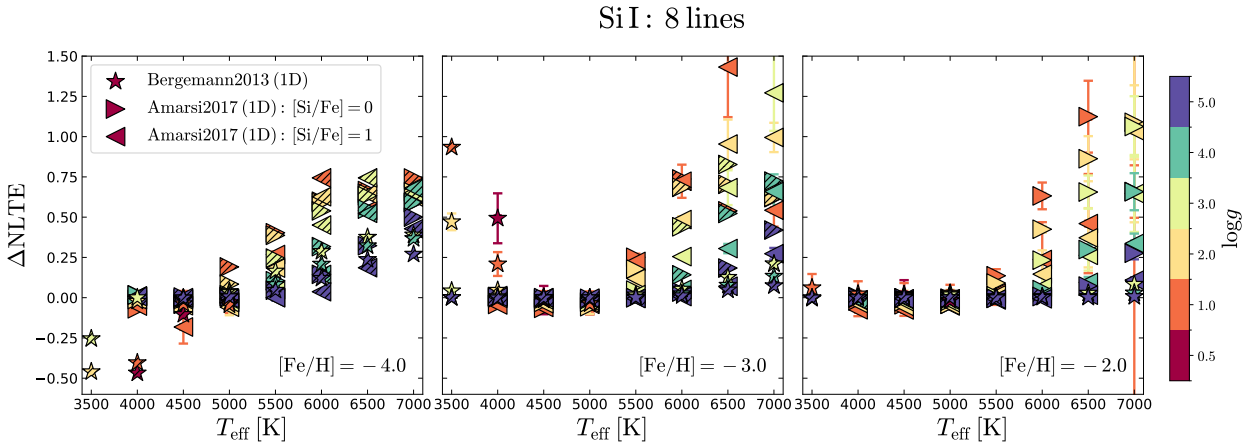

Fig. B.3: Same as Fig. B.1 for Si I. Star symbols and triangles show the 1D NLTE corrections by Bergemann et al. (2013) and Amarsi & Asplund (2017), respectively. Diagonally hatched symbols show cases where only one line is detectable (other lines are too weak, EW < 5 mÅ), in this case the resonance Si I line at 3906Å.

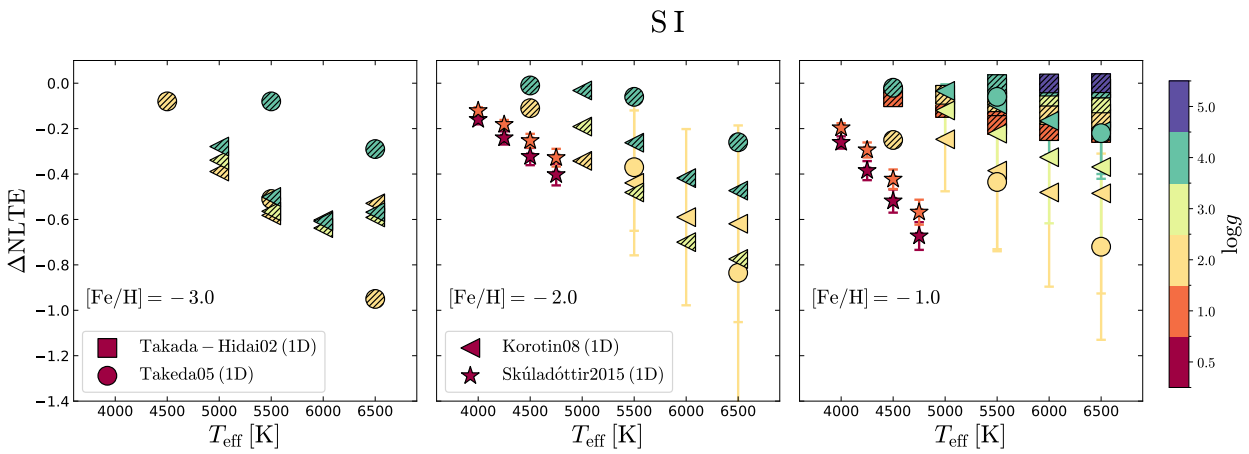

Fig. B.4: Same as Fig. B.3 for S I. Squares show the corrections of Takada-Hidai et al. (2002) for the 8694 Å line; stars show the average corrections of the S I triplet at 9213, 9228 and 9238 Å from Skúladóttir et al. (2015); circles show the average corrections of the 8694 and 9213 Å lines from Takeda et al. (2005); and triangles the average corrections of the 8694, 9213 and the 8th S I multiple at 6543-6557 Å from Korotin (2008). Diagonally hatched symbols represent cases where only one line is available, which is the 9213 Å line for the Takeda et al. (2005) and Korotin (2008) grids at [Fe/H] ≤ −2; and the 8694 Å line for the Takada-Hidai et al. (2002) line at [Fe/H] = −1.

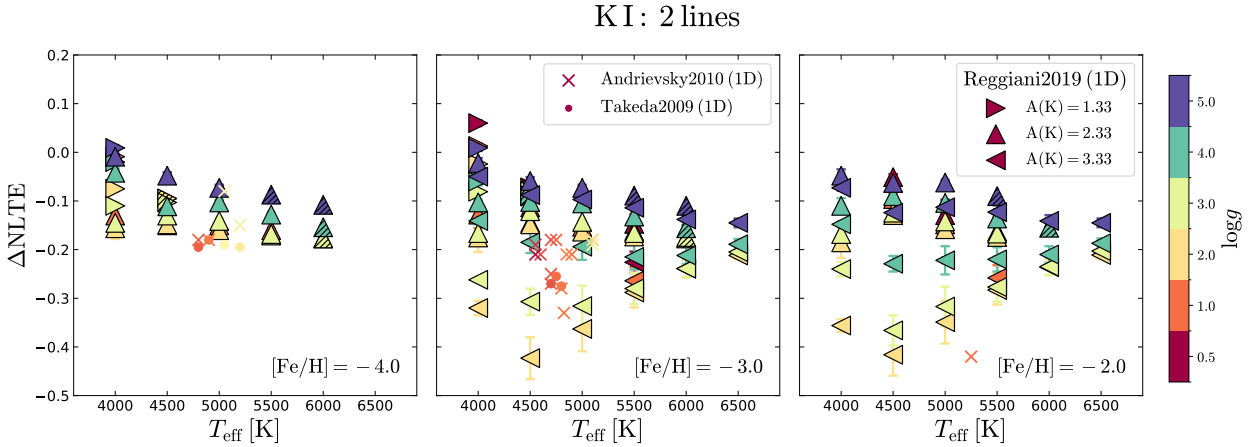

Fig. B.5: Same as Fig. B.3 for K I. Triangles show 1D NLTE corrections by Reggiani et al. (2019) for three different K abundances, A(K)=1.33, 2.33 and 3.33 ($A(K)_\odot$ = 5.03). NLTE corrections for individual stars by Andrievsky et al. (2010) are shown as X symbols, and from Takeda et al. (2009) as circles.

Fig. D.3 displays [K/Fe], [Ti I/Fe], and [Ti II/Fe] as a function of [Fe/H]. We find that the observed LTE distributions of K and Ti lie ∼ 1 dex and ∼ 0.6 dex higher than our model predictions at −2 ≤ [Fe/H] ≤ −1. These discrepancies are consistent with previous findings that theoretical models systematically underproduce these elements compared to observations at all metallicities (see, e.g., Nomoto et al. 2013; Kobayashi et al. 2020). The negative NLTE corrections for [K/Fe] decrease the scatter of the distribution from $\sigma_{\rm LTE}$ = 0.24 to $\sigma_{\rm NLTE}$ = 0.21 and lower its peak by 0.4 dex. However, the observed distribution still lies on the high end of our model predictions. Substituting the Reggiani et al. (2019) corrections with those of Takeda et al. (2002) - which differ by less than 0.1 dex for stars where both grids are defined - lowers the peak by an additional 0.1 dex, resulting in limited improvement. In contrast, the corrections for [Ti I/Fe] shift the peak upwards by 0.4 dex, further exacerbating the discrepancy with model predictions. The situation is similar for [Ti II/Fe], where the LTE peak is 0.1 dex higher than that of [Ti I/Fe] and remains unchanged in NLTE.

Finally, Fig. D.4 shows the distributions of [Co/Fe], [Cu/Fe] and [Zn/Fe] as a function of [Fe/H]. We find that in LTE, the observed [Co/Fe] distribution lies on the high side of our model predictions. Applying NLTE corrections causes a shift of +0.6 dex, raising the entire distribution above the predicted one. Furthermore, the scatter is increased from $\sigma_{\rm LTE}$ = 0.24 to $\sigma_{\rm NLTE}$ = 0.30, owing to a downward trend of [Co/Fe] with [Fe/H] that appears in NLTE.

The observed [Cu/Fe] distribution aligns well with our model in LTE, while the NLTE corrections shift its peak by +0.4 dex, moving it towards the high side of our predictions. In addition, the distribution becomes flatter and even shows an upturn in the [Cu/Fe] trend at [Fe/H] ≲ −2, in agreement with recent calcula-

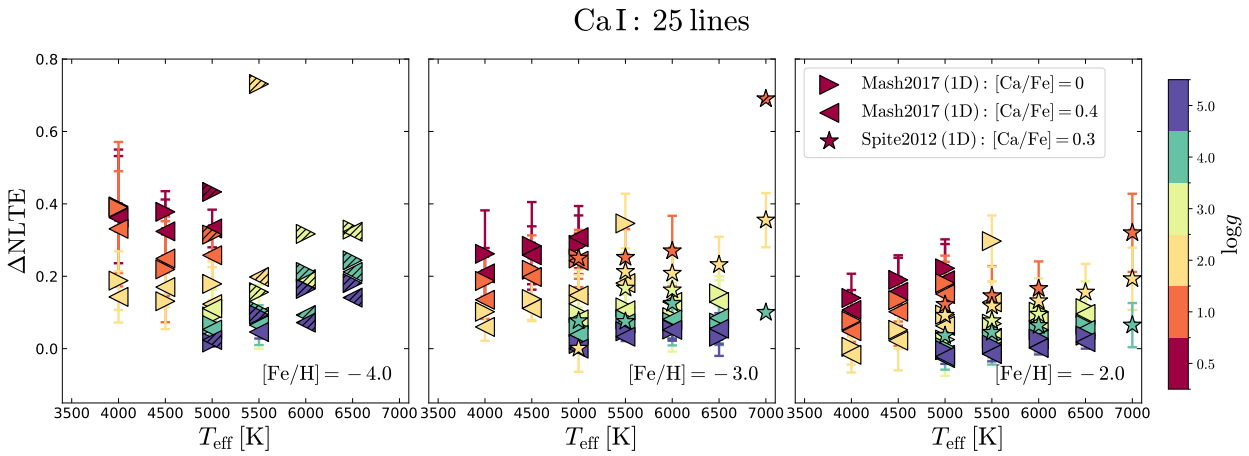

Fig. B.6: Same as Fig. B.3 for Ca I. Triangles and star symbols show 1D NLTE corrections from Mashonkina et al. (2007) and Spite et al. (2012), respectively. Symbols are hatched diagonally where only one line is available in the range 5 mÅ < EW < 200 mÅ.

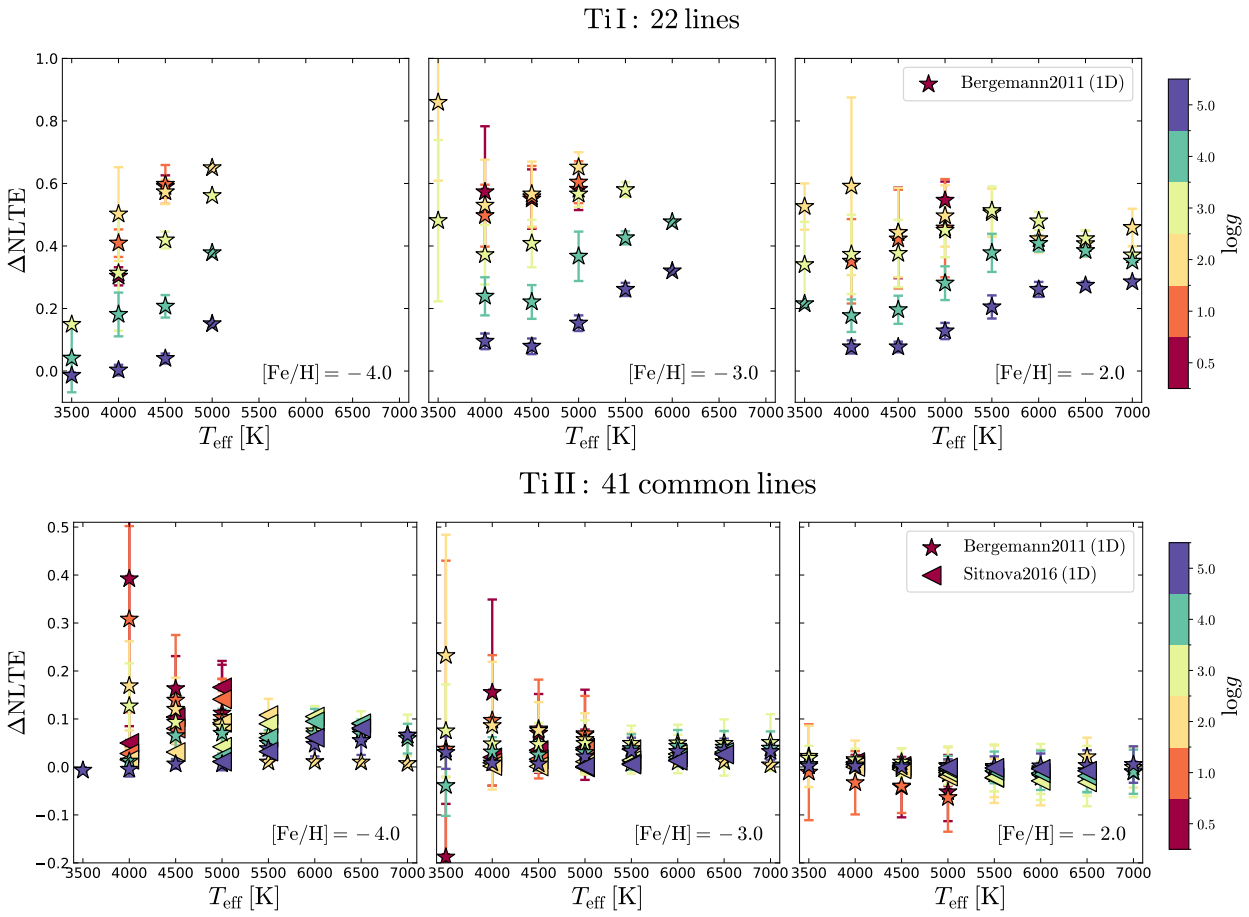

Fig. B.7: Same as Fig. B.3 for Ti I (top) and Ti II (bottom). Star symbols and triangles show the 1D NLTE corrections by Bergemann (2011) and Sitnova et al. (2016), respectively.

tions of NLTE Cu abundances in the Milky Way halo (Caliskan et al. 2025).

The observed distribution of Zn lies on the high end of our model predictions. This issue is similarly reported in Rossi et al. (2024), who also use the Limongi & Chieffi (2018) Pop II yields, but not in Kobayashi et al. (2020) who use a different set of yields and a large fraction (= 50%) of Pop II hypernovae. Indeed, the Limongi & Chieffi (2018) yields for ccSNe predict a [Zn/Fe] < 0 at all masses, lower than in other published sets (see Fig. 5 of Nomoto et al. 2013). The NLTE corrections here, are minimal and do not improve the agreement; the peak is shifted by +0.1 dex and the scatter is slightly decreased. Note that the

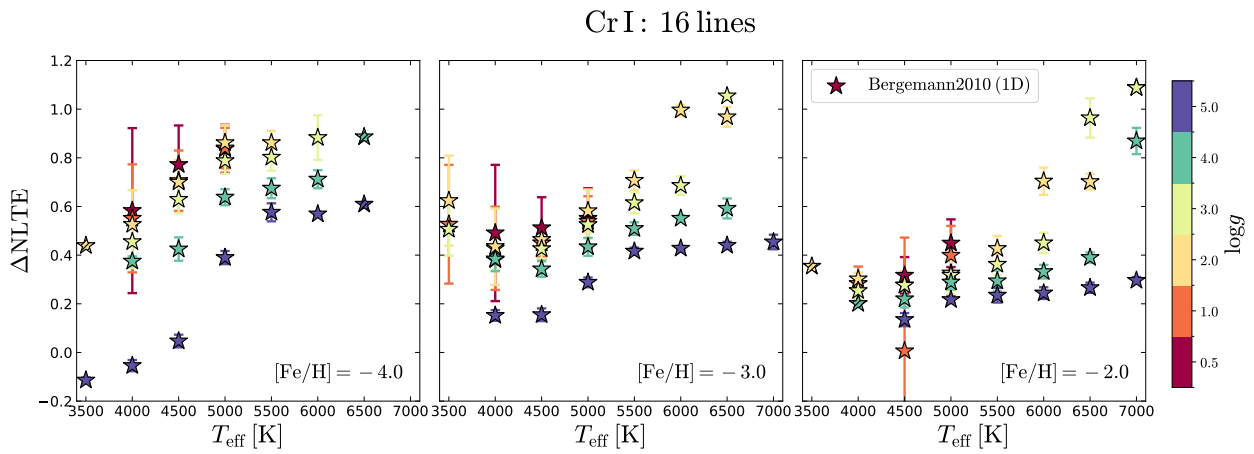

Fig. B.8: Same as Fig. B.3 for Cr I, using the 1D NLTE corrections by Bergemann & Cescutti (2010). Error bars represent the standard deviation.

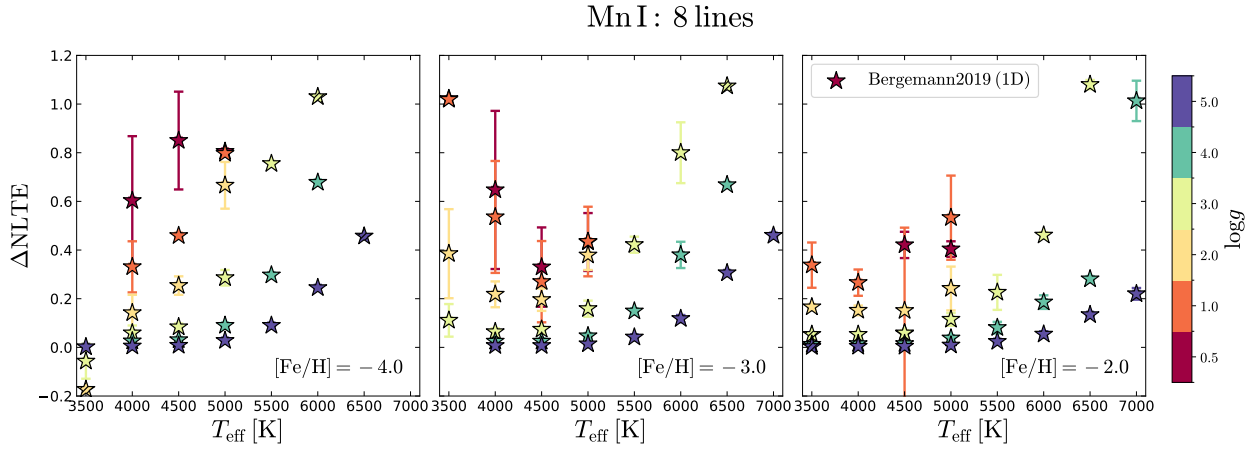

Fig. B.9: Same as Fig. B.3 for Mn I. Star symbols show 1D NLTE corrections by Bergemann et al. (2019).

predicted distributions for [Cu/Fe] and [Zn/Fe] are significantly extended due to the inclusion of zero-metallicity PISNe, which yield very low abundance ratios for these elements (e.g. Salvadori et al. 2019). This primarily affects the light gray area, representing Pop III descendants ($\geq$ 50%), but also the dark gray area (Pop II descendants, > 50%) in the case of significant Pop III contribution.

References

Alexeeva, S. A., Pakhomov, Y. V., & Mashonkina, L. I. 2014, Astronomy Letters, 40, 406
Amarsi, A. M. & Asplund, M. 2017, MNRAS, 464, 264
Amarsi, A. M., Liljegren, S., & Nissen, P. E. 2022, A&A, 668, A68
Amarsi, A. M., Nissen, P. E., & Skúladóttir, Á. 2019, A&A, 630, A104
Andrievsky, S., Bonifacio, P., Caffau, E., et al. 2018, MNRAS, 473, 3377
Andrievsky, S. M., Spite, M., Korotin, S. A., et al. 2010, A&A, 509, A88
Bergemann, M. 2011, MNRAS, 413, 2184
Bergemann, M. & Cescutti, G. 2010, A&A, 522, A9
Bergemann, M., Collet, R., Amarsi, A. M., et al. 2017, ApJ, 847, 15
Bergemann, M., Gallagher, A. J., Eitner, P., et al. 2019, A&A, 631, A80
Bergemann, M., Hansen, C. J., Bautista, M., & Ruchti, G. 2012a, A&A, 546, A90
Bergemann, M., Hoppe, R., Semenova, E., et al. 2021, MNRAS, 508, 2236
Bergemann, M., Kudritzki, R.-P., Würl, M., et al. 2013, ApJ, 764, 115
Bergemann, M., Lind, K., Collet, R., Magic, Z., & Asplund, M. 2012b, MNRAS, 427, 27
Bergemann, M., Pickering, J. C., & Gehren, T. 2010, MNRAS, 401, 1334
Caliskan, S., Amarsi, A. M., Racca, M., et al. 2025, A&A, 696, A210
Eitner, P., Bergemann, M., Ruiter, A. J., et al. 2023, A&A, 677, A151
Fabbian, D., Asplund, M., Barklem, P. S., Carlsson, M., & Kiselman, D. 2009, A&A, 500, 1221
Fulbright, J. P. & Johnson, J. A. 2003, ApJ, 595, 1154
Gallagher, A. J., Bergemann, M., Collet, R., et al. 2020, A&A, 634, A55
Gratton, R. G., Carretta, E., Eriksson, K., & Gustafsson, B. 1999, A&A, 350, 955
Gratton, R. G., Sneden, C., Carretta, E., & Bragaglia, A. 2000, A&A, 354, 169
Kobayashi, C., Karakas, A. I., & Lugaro, M. 2020, ApJ, 900, 179
Korotin, S. A. 2008, Odessa Astronomical Publications, 21, 42
Korotin, S. A., Andrievsky, S. M., Hansen, C. J., et al. 2015, A&A, 581, A70
Limongi, M. & Chieffi, A. 2018, ApJS, 237, 13
Lind, K., Asplund, M., & Barklem, P. S. 2009, A&A, 503, 541
Lind, K., Asplund, M., Barklem, P. S., & Belyaev, A. K. 2011, A&A, 528, A103
Lind, K., Nordlander, T., Wehrhahn, A., et al. 2022, A&A, 665, A33
Mashonkina, L. 2013, A&A, 550, A28
Mashonkina, L. & Gehren, T. 2000, A&A, 364, 249
Mashonkina, L., Gehren, T., Shi, J. R., Korn, A. J., & Grupp, F. 2011, A&A, 528, A87
Mashonkina, L., Korn, A. J., & Przybilla, N. 2007, A&A, 461, 261
Mashonkina, L., Pakhomov, Y. V., Sitnova, T., et al. 2022, MNRAS, 509, 3626
Mashonkina, L., Sitnova, T., & Belyaev, A. K. 2017, A&A, 605, A53
Mashonkina, L. I. & Belyaev, A. K. 2019, Astronomy Letters, 45, 341
Matsuno, T., Amarsi, A. M., Carlos, M., & Nissen, P. E. 2024, A&A, 688, A72
Merle, T., Thévenin, F., Pichon, B., & Bigot, L. 2011, MNRAS, 418, 863
Nomoto, K., Kobayashi, C., & Tominaga, N. 2013, ARA&A, 51, 457
Nordlander, T. & Lind, K. 2017, A&A, 607, A75

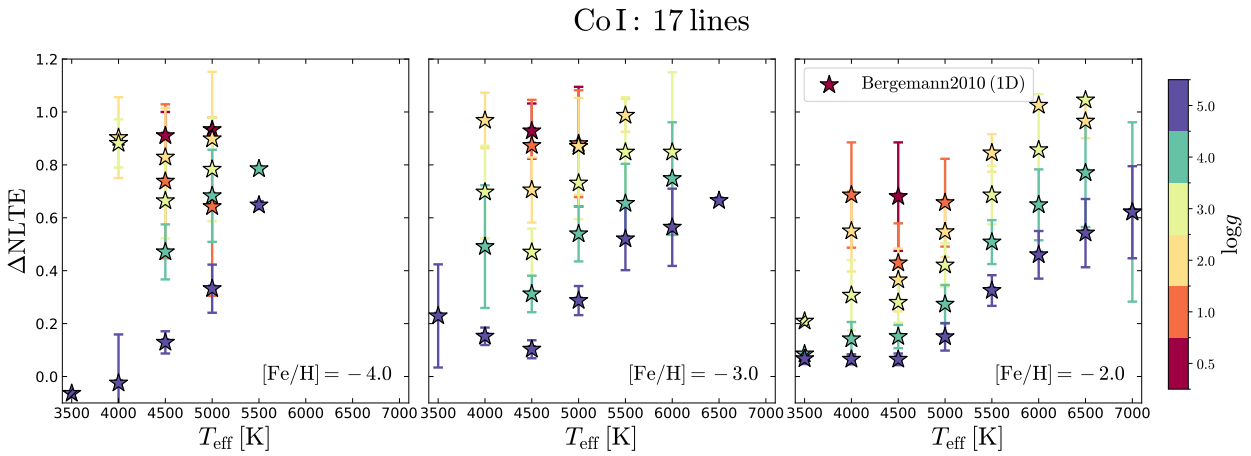

Fig. B.10: Same as Fig. B.3 for Co I, using the 1D NLTE corrections by Bergemann et al. (2010).

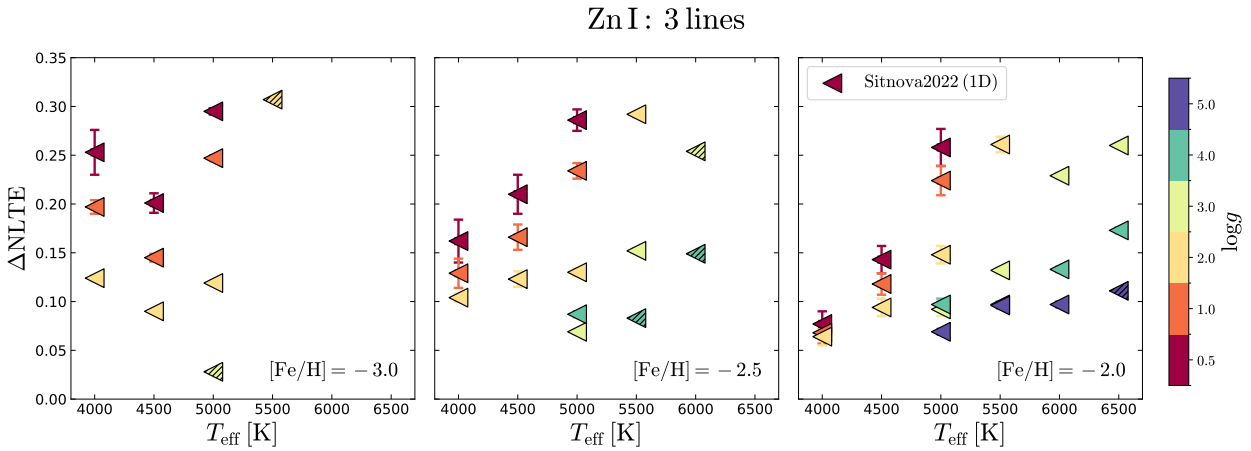

Fig. B.11: Same as Fig. B.3 for Zn I using the 1D NLTE corrections by Sitnova et al. (2022).

Norris, J. E. & Yong, D. 2019, ApJ, 879, 37
Osorio, Y. & Barklem, P. S. 2016, A&A, 586, A120
Reggiani, H., Amarsi, A. M., Lind, K., et al. 2019, A&A, 627, A177
Roederer, I. U., Preston, G. W., Thompson, I. B., et al. 2014, AJ, 147, 136
Rossi, M., Salvadori, S., Skúladóttir, Á., Vanni, I., & Koutsouridou, I. 2024, ApJ (accepted), arXiv:2406.12960
Salvadori, S., Bonifacio, P., Caffau, E., et al. 2019, MNRAS, 487, 4261
Sbordone, L., Bonifacio, P., Caffau, E., et al. 2010, A&A, 522, A26
Shi, J. R., Yan, H. L., Zhou, Z. M., & Zhao, G. 2018, ApJ, 862, 71
Sitnova, T. M., Mashonkina, L. I., & Ryabchikova, T. A. 2016, MNRAS, 461, 1000
Sitnova, T. M., Yakovleva, S. A., Belyaev, A. K., & Mashonkina, L. I. 2022, MNRAS, 515, 1510
Skúladóttir, Á., Andrievsky, S. M., Tolstoy, E., et al. 2015, A&A, 580, A129
Spite, M., Andrievsky, S. M., Spite, F., et al. 2012, A&A, 541, A143
Takada-Hidai, M., Takeda, Y., Sato, S., et al. 2002, ApJ, 573, 614
Takeda, Y., Hashimoto, O., Taguchi, H., et al. 2005, PASJ, 57, 751
Takeda, Y., Kaneko, H., Matsumoto, N., et al. 2009, PASJ, 61, 563
Takeda, Y., Takada-Hidai, M., Sato, S., et al. 2000, arXiv e-prints, astro
Takeda, Y., Zhao, G., Chen, Y.-Q., Qiu, H.-M., & Takada-Hidai, M. 2002, PASJ, 54, 275
Wang, E. X., Nordlander, T., Asplund, M., et al. 2021, MNRAS, 500, 2159
Xu, X., Shi, J., & Wang, X. 2022, ApJ, 936, 4

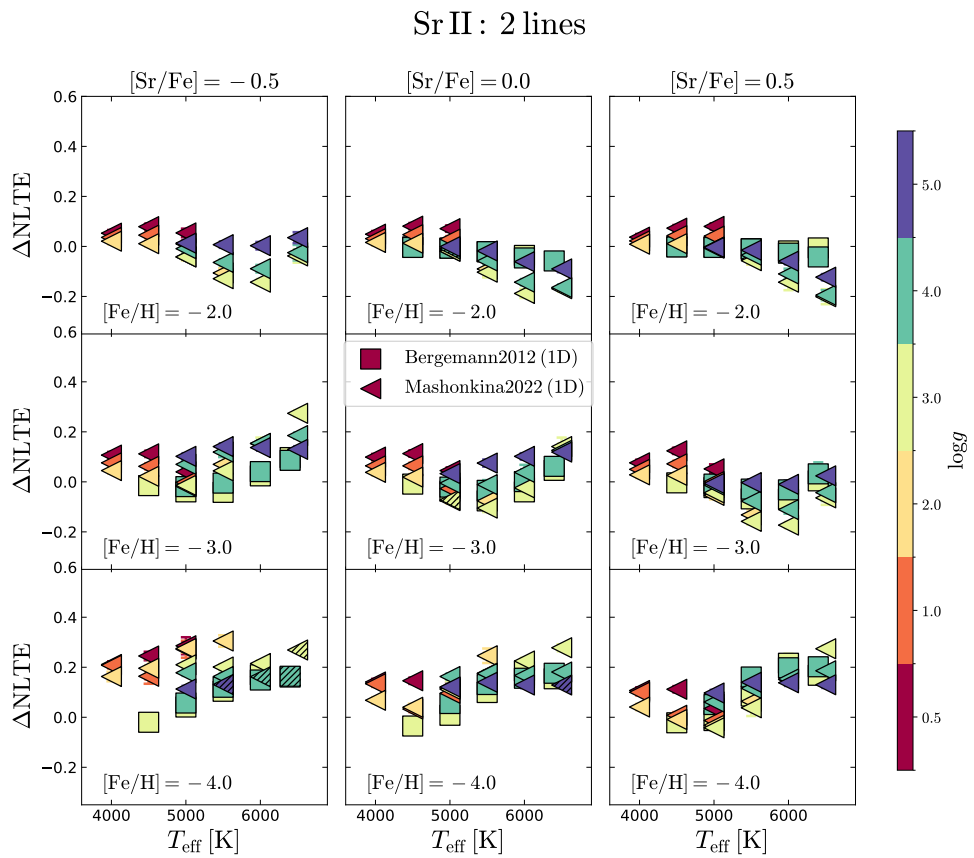

Fig. B.12: Same as Fig. B.3 for Sr II. Squares and triangles show 1D NLTE corrections by Bergemann et al. (2012a) and Mashonkina et al. (2022), respectively. Columns show different [Sr II/Fe] values: [Sr II/Fe] = −0.5 (left), 0 (middle) and +0.5 (right).

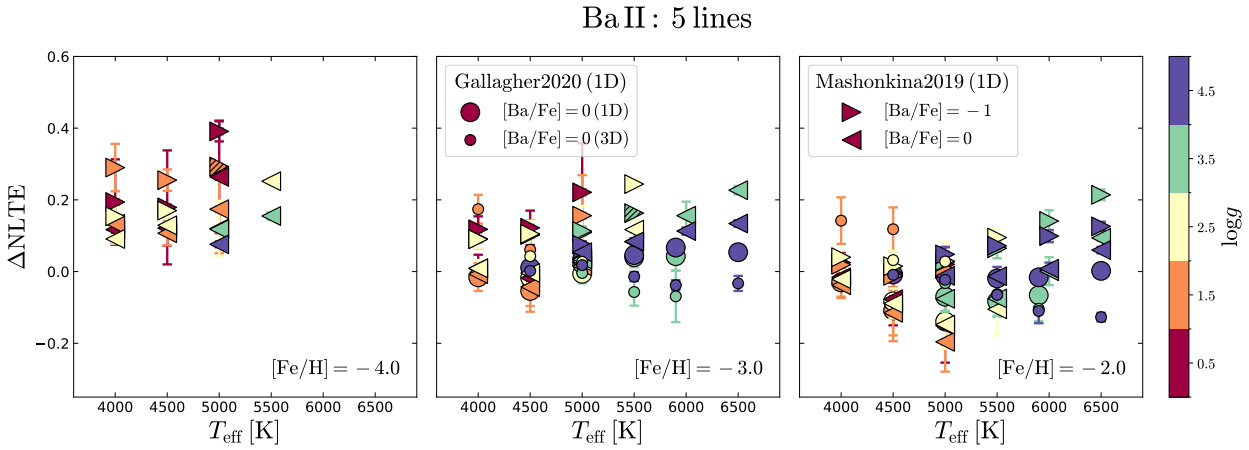

Fig. B.13: Same as Fig. B.3 for Ba II. Triangles show the 1D NLTE corrections by Mashonkina & Belyaev (2019) and circles the 1D and 3D NLTE corrections by Gallagher et al. (2020).

Table A.1: The 1D and 3D NLTE grids included in NLiTE.

			Grid range				
Species	Authors	Type	$T_{\rm eff}$	log$g$	[Fe/H]	[X/Fe]	A(X)
Li I	Lind et al. (2009)	1D NLTE	[4000,8000]	[1,5]	$[-3, 0]$	-	$[-0.3, 4.2]$
Li I	Sbordone et al. (2010)	1D/3D NLTE	[5500,6500]	[3.5,4.5]	$[-3, -2]$	-	$[1.2, 3.3]$
Li I	Wang et al. (2021)	3D NLTE*	[4000,7000]	[1.5,5]	$[-4, 0.5]$	-	$[-0.5, 4]$
CH	Norris & Yong (2019)	3D NLTE*	-	-	$[-6, -1]$	-	-
C I	Amarsi et al. (2019)	1D NLTE*	$[4000, 7500]$	$[0, 5]$	$[-5, 0]$	$[-0.4, 1.2]$	-
		3D NLTE	$[5000, 6500]$	$[3, 5]$	$[-3, 0]$		
O I	Amarsi et al. (2019)	1D NLTE*	$[4000, 7500]$	$[0, 5]$	$[-5, 0]$	$[-0.4, 1.2]$	-
		3D NLTE	$[5000, 6500]$	$[3, 5]$	$[-3, 0]$		
O I	Bergemann et al. (2021)	1D NLTE	[4000,7500]	[0.5,5]	$[-2.5, -1]$	-	-
Na I	Lind et al. (2011)	1D NLTE	[4000,6500]	[1,5]	$[-5, -1]$	$[-0.6, 0.6]$	-
Na I	Alexeeva et al. (2014)	1D NLTE	[4000,6500]	[0.5,5]	$[-5, -2]$	$[-0.6, 0.6]$	-
Na I	Lind et al. (2022)	1D NLTE*	[4000,7500]	[0,5]	$[-5, -0.5]$	$[-1, 0.8]$	-
Mg I	Merle et al. (2011)	1D NLTE	[3500,5250]	[0.5,2]	$[-4, -1]$	-	-
Mg I	Mashonkina (2013)	1D NLTE	[4000,6500]	[0.5,5]	$[-5, -2]$	-	-
Mg I	Osorio & Barklem (2016)	1D NLTE*	[3500,7500]	[0.5,5]	$[-5, -1]$	-	[2.6,8.6]
Mg I	Bergemann et al. (2017)	1D NLTE	[3500,7500]	[0.5,5]	$[-5, -1]$	-	-
Mg I	Lind et al. (2022)	1D NLTE	[4000,7500]	[0,5]	$[-5, -0.5]$	$[-1, 0.8]$	-
Mg I	Matsuno et al. (2024)	1D/3D NLTE	[5000,6500]	[4,5]	-	-	[5,7.6]
Al I	Nordlander & Lind (2017)	1D NLTE	$[4000, 7500]$	$[0, 5]$	$[-4, -0.5]$	$[-2, 1.9]$	-
		$\langle$3D$\rangle$ NLTE	$[4000, 7000]$	$[1.5, 5]$			
Al I	Lind et al. (2022)	1D NLTE*	[4000,7500]	[0,5]	$[-5, -0.5]$	$[-1, 0.8]$	-
Si I	Bergemann et al. (2013)	1D NLTE	[3500,7500]	[0.5,5]	$[-5, -1]$	-	-
Si I	Amarsi & Asplund (2017)	1D NLTE*	[4000,7500]	[1,5]	$[-5, -1]$	$[-0.5, 1.5]$	-
S I	Takada-Hidai et al. (2002)	1D NLTE	[4500,6500]	[1,5]	$[-2, 0]$	$[-0.2, 1.2]$	-
S I	Takeda et al. (2005)	1D NLTE	[4500,6500]	[2,4]	$[-3, 0]$	-	-
S I	Korotin (2008)	1D NLTE	[5000,6500]	[2,4]	$[-3, 0]$	-	-
S I	Skúladóttir et al. (2015)	1D NLTE	[4000,4750]	[0,1.5]	$[-2.5, -1]$	[0,0.6]	-
K I	Takeda et al. (2002)	1D NLTE	[4500,6500]	[1,5]	$[-3, 0]$	-	[2.55,6.54]
K I	Reggiani et al. (2019)	1D NLTE*	[4000,8000]	[0,5]	$[-5, 0.5]$	-	[0.08,6.83]
Ca I	Spite et al. (2012)	1D NLTE	[4750,7000]	[1,4]	$[-3.5, -1]$	[0,0.3]	-
Ca I	Mashonkina et al. (2017)	1D NLTE*	[4000,6500]	[0.5,5]	$[-5, -2]$	[0,0.4]	-
Ti I	Bergemann (2011)	1D NLTE*	[3500,7500]	[0.5,5]	$[-5, -1]$	-	-
Ti II	Bergemann (2011)	1D NLTE*	[3500,7500]	[0.5,5]	$[-5, -1]$	-	-
Ti II	Sitnova et al. (2016)	1D NLTE	[4000,6500]	[0.5,5]	$[-4, 0]$	-	-
Cr I	Bergemann & Cescutti (2010)	1D NLTE*	[3500,7500]	[0.5,5]	$[-5, -1]$	-	-
Mn I	Bergemann et al. (2019)	1D NLTE*	[3500,7500]	[0.5,5]	$[-5, -1]$	-	-
Fe I	Mean corrections from Mashonkina et al. (2011) & Bergemann et al. (2012b)	1D NLTE*	[3500,7500]	[0.5,5]	$[-5, -1]$	-	-
Fe I	Mashonkina et al. (2011)	1D NLTE	[4000,6500]	[0.5,5]	$[-5, -2]$	-	-
Fe I	Bergemann et al. (2012b)	1D NLTE	[3500,7500]	[0.5,5]	$[-5, -1]$	-	-
Fe I	Amarsi et al. (2022)	3D NLTE	[5000,6500]	[4,4.5]	$[-3, -1]$	-	-

Table A.1: (Continued)

Species	Authors	Type	Grid range				
			$T_{\rm eff}$	log$g$	[Fe/H]	[X/Fe]	A(X)
Fe II	Bergemann et al. (2012b)	1D NLTE⋆	[3500,7500]	[0.5,5]	[−5, −1]	-	-
Fe II	Amarsi et al. (2019)	3D LTE	[4000,6500]	[1.5,5]	[−4, −1]	-	-
Fe II	Amarsi et al. (2022)	3D NLTE	[5000,6500]	[4,4.5]	[−3, −1]	-	-
Co I	Bergemann et al. (2010)	1D NLTE⋆	[3500,7500]	[0.5,5]	[−5, −1]	-	-
Ni I	Eitner et al. (2023)	1D NLTE⋆	[5000,6500]	[3,4.5]	[−3, 0]	-	-
Cu I	Andrievsky et al. (2018) & Shi et al. (2018) & Xu et al. (2022)	1D NLTE⋆	-	-	[−4.2, −1]	-	-
Zn I	Sitnova et al. (2022)	1D NLTE⋆	[4000,6500]	[0.5,5]	[−3.5, 0]	-	-
Sr II	Mashonkina et al. (2022)	1D NLTE⋆	[4000,6500]	[0.5,5]	[−5, −2]	[−1.5, 1]	-
Sr II	Bergemann et al. (2012a)	1D NLTE	[4500,6400]	[2.2,4]	[−3.9, −1]	[−0.5, 0.5]	-
Ba II	Mashonkina & Belyaev (2019)	1D NLTE⋆	[4000,6500]	[0.5,5]	[−5, −2]	[−1.5, 0.5]	-
Ba II	Gallagher et al. (2020)	1D/3D NLTE	[4000,6500]	[1.5,4.5]	[−3, −1]	[−2.5, 2]	-
Ba II	Korotin et al. (2015)	1D NLTE	[4000,6500]	[0.5,5]	[−2, −1]	[−0.2, 0.4]	-
Eu II	Mashonkina & Gehren (2000)	1D NLTE⋆	[4000,5750]	[0.5,3]	[−3, −2]	[−0.5, 1.5]	-

Note: ⋆ denotes our fiducial NLTE grid for each element.

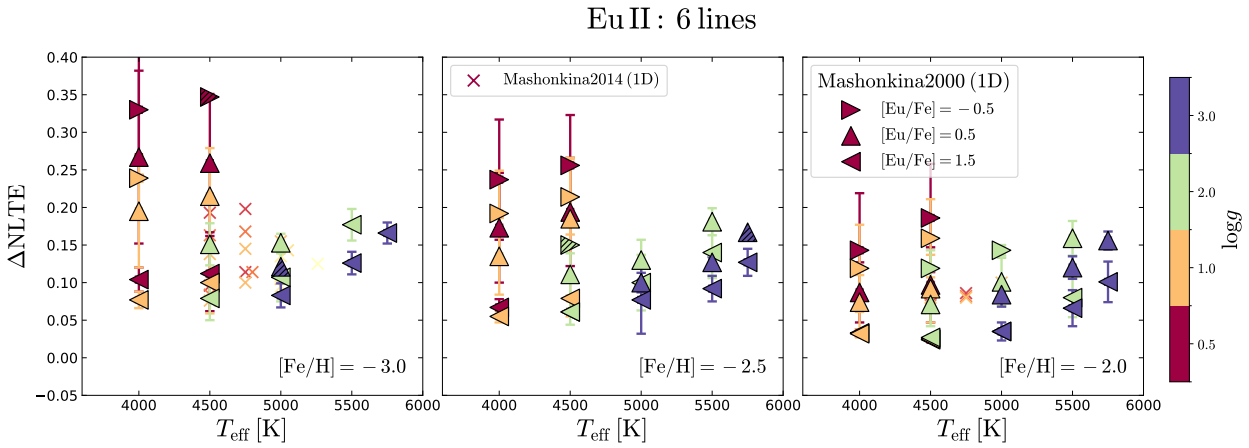

Fig. B.14: Same as Fig. B.3 for Eu II using the 1D NLTE corrections by Mashonkina & Gehren (2000).

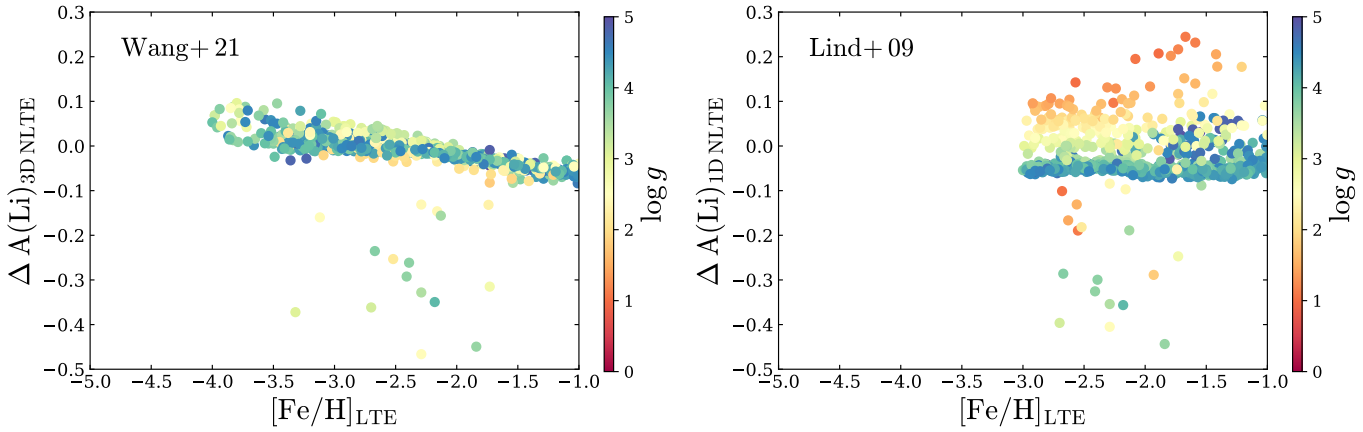

Fig. C.1: NLTE corrections for A(Li I), for MP SAGA stars as a function of their [Fe/H]$_{\rm LTE}$, color-coded according to their log g values. Li has been corrected using the 3D NLTE corrections from our fiducial grid of Wang et al. (2021; left), and the 1D NLTE corrections from Lind et al. (2009; right). Only stars with stellar parameters within the respective grid limits are shown.

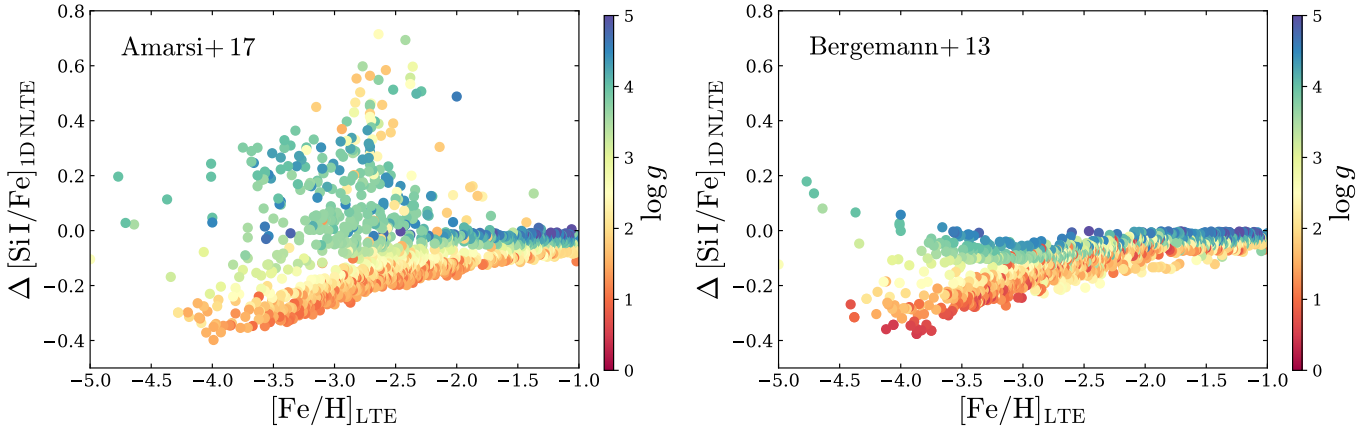

Fig. C.2: Net NLTE corrections for [Si I/Fe] in MP SAGA stars, as a function of [Fe/H]$_{\rm LTE}$, color-coded according to log g. Two sets of Si 1D NLTE corrections are shown, from our fiducial grid of Amarsi & Asplund (2017; left), and that of Bergemann et al. (2013; right). The 1D NLTE corrections for Fe I are the mean of the grids of Mashonkina et al. (2011) and Bergemann et al. (2012b) in both panels. Only stars with stellar parameters within the respective grid limits are shown.

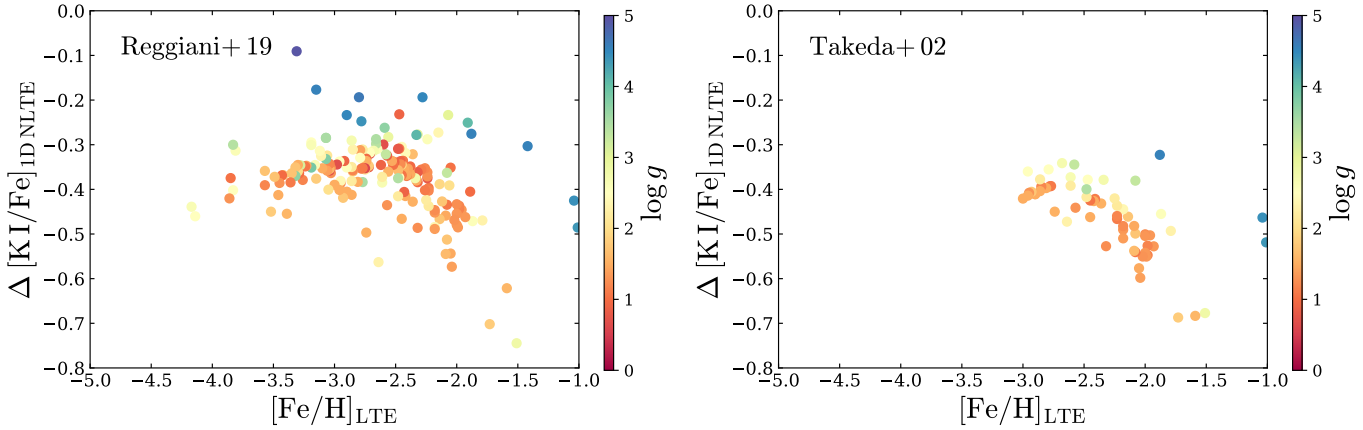

Fig. C.3: Same as Fig. C.2 for [K I/Fe], using our fiducial grid of Reggiani et al. (2019; left), and that of Takeda et al. (2002;right).

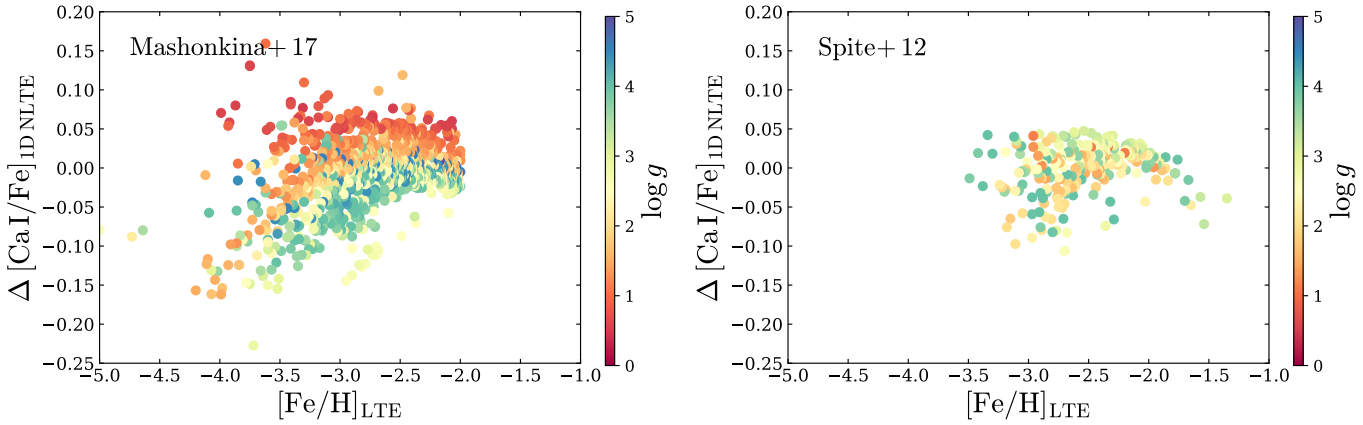

Fig. C.4: Same as Fig. C.2 for [Ca I/Fe] using our fiducial grid from Mashonkina et al. (2017; left) and Spite et al. (2012; right).

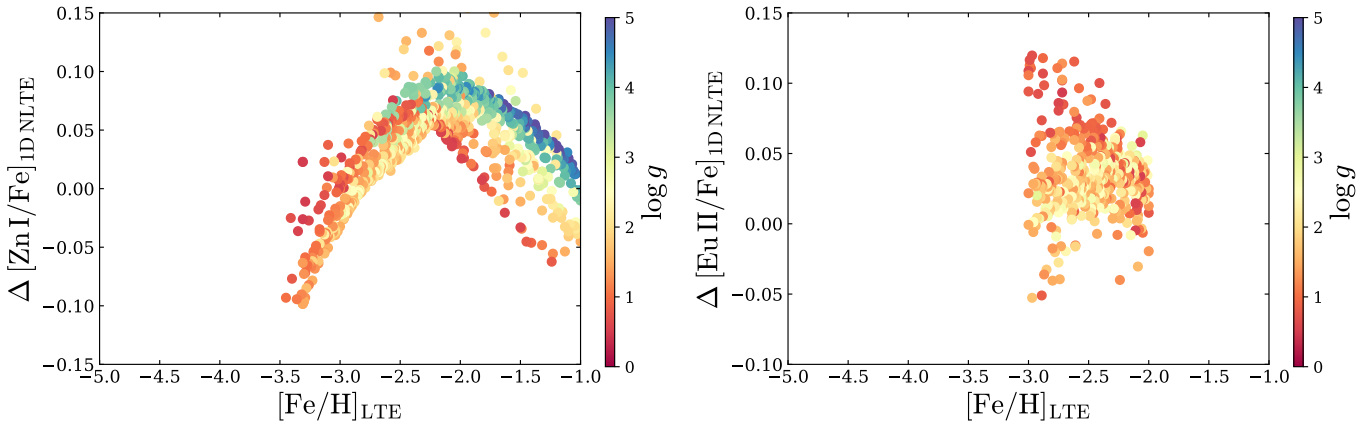

Fig. C.5: Same as Fig. C.2 for [Zn I/Fe] (left), and [Eu II/Fe] (right), using the 1D NLTE corrections from Sitnova et al. (2022), and Mashonkina & Gehren (2000), respectively.

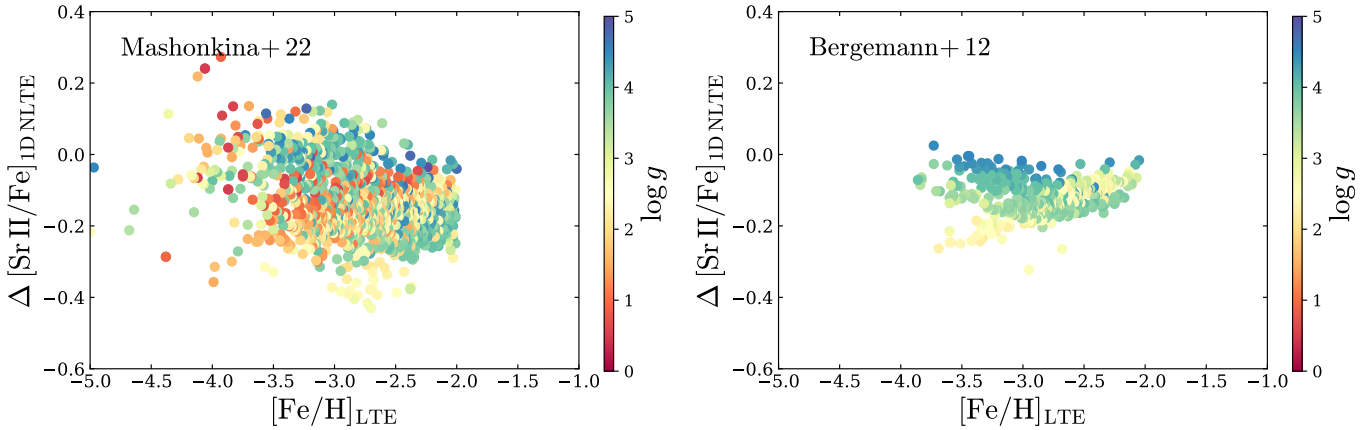

Fig. C.6: Same as Fig. C.2 for [Sr II/Fe], using our fiducial grid of Mashonkina et al. (2022; left), and the grid from Bergemann et al. (2012a; right).

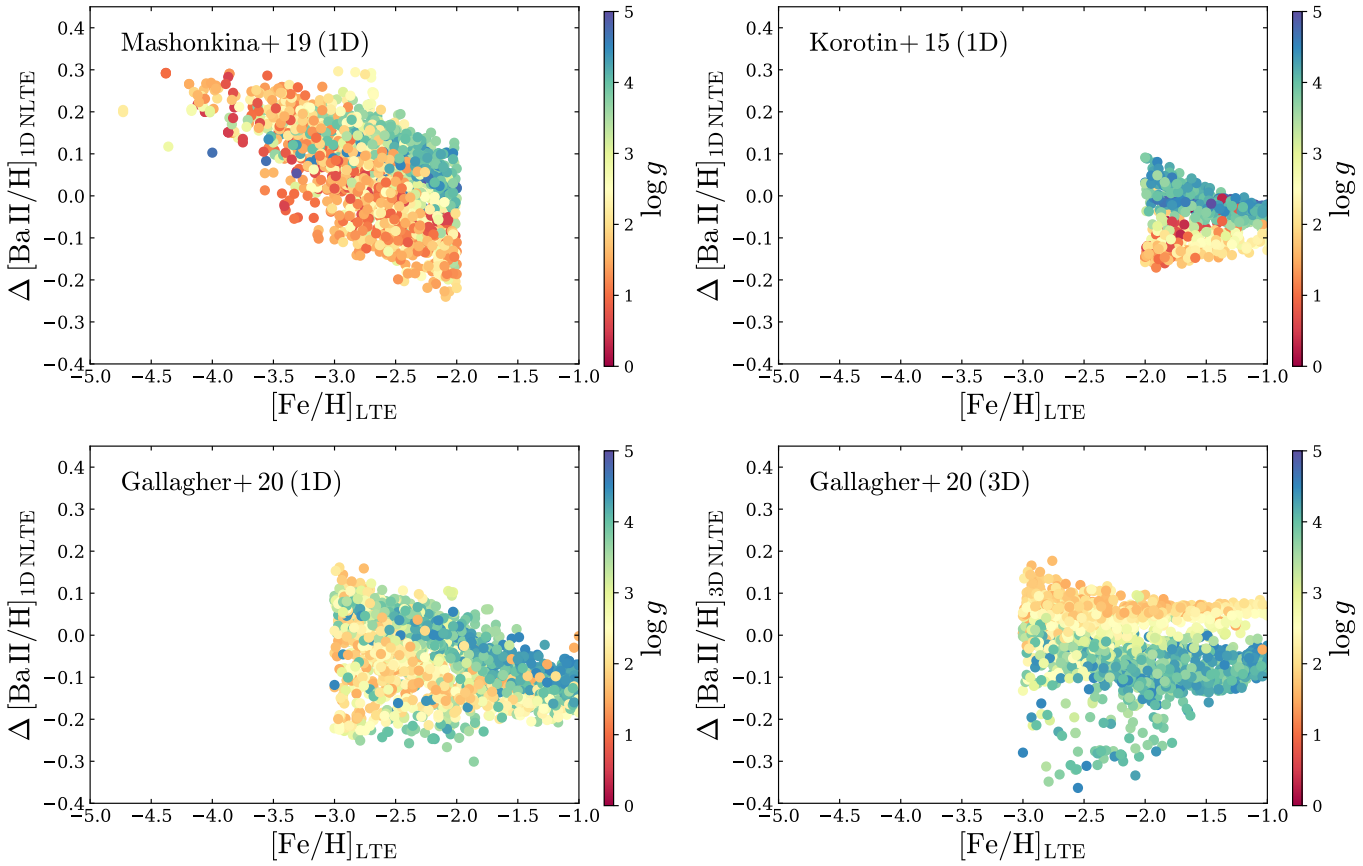

Fig. C.7: Same as Fig. C.2 for [Ba II/H], based on the fiducial 1D NLTE corrections from Mashonkina & Belyaev (2019; top left), as well as those of Korotin et al. (2015; top right); and finally the 1D (bottom-left) and 3D (bottom-left) NLTE corrections from Gallagher et al. (2020).

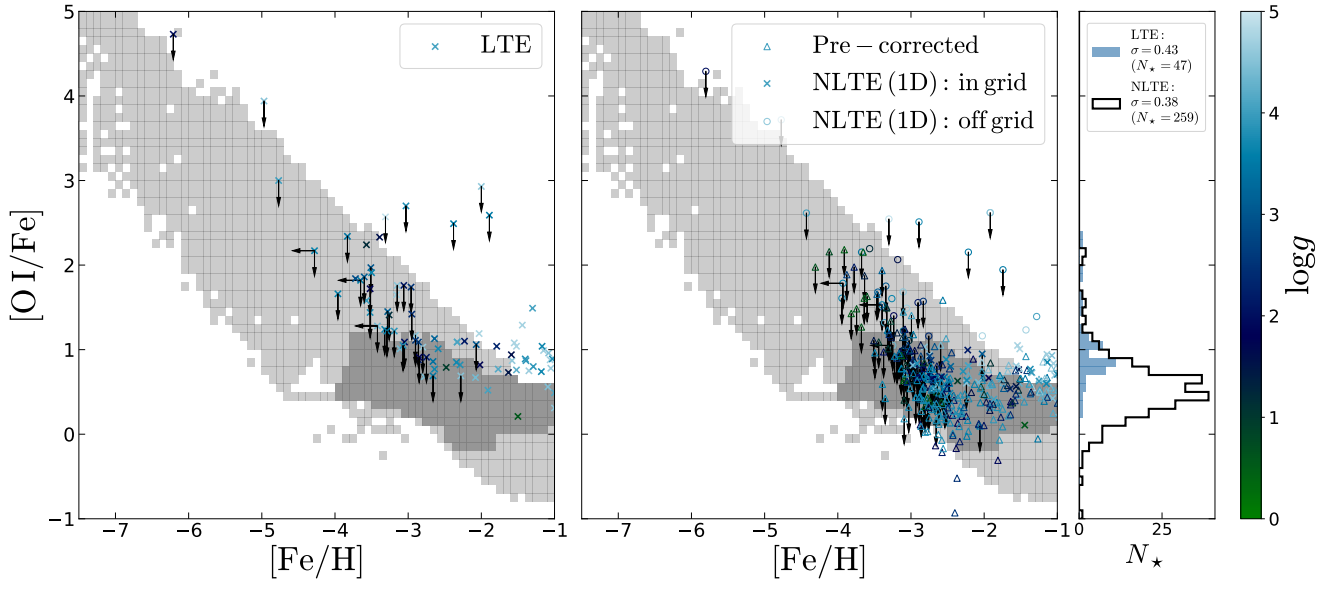

Fig. D.1: Same as Fig. 22 for [O I/Fe]; observed abundances have been corrected using the grid of Amarsi et al. (2019) for O I and the mean corrections of Mashonkina et al. (2011) and Bergemann et al. (2012b) for Fe I.

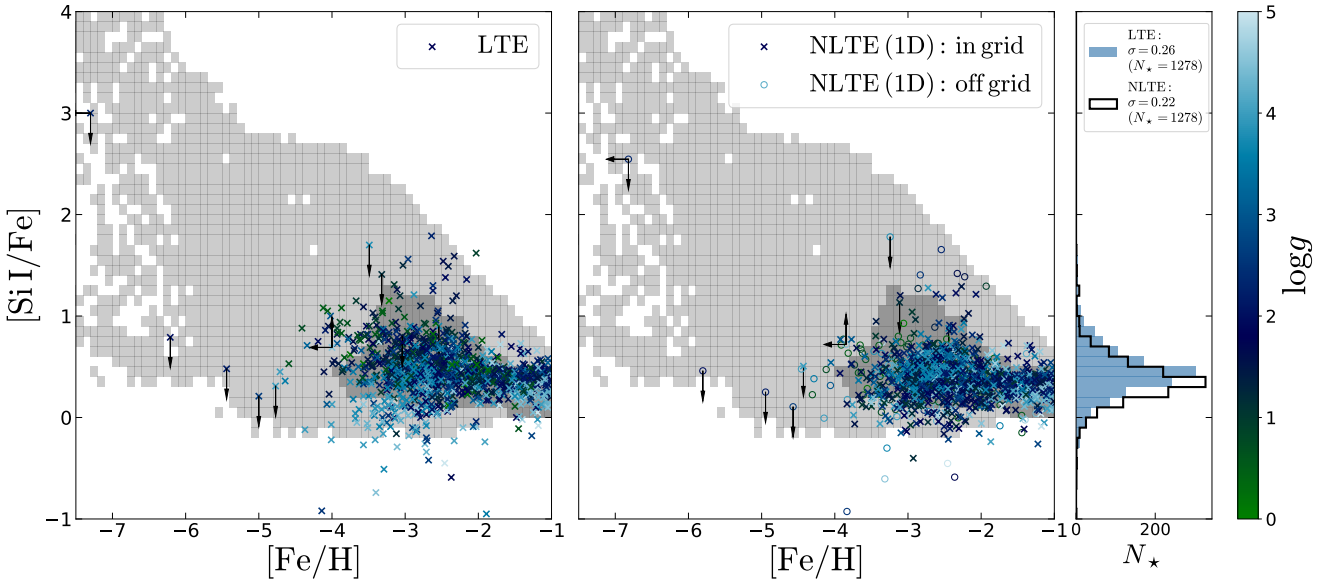

Fig. D.2: Same as Fig. 22 for [Si/Fe]; observed abundances have been corrected using the grid from Amarsi & Asplund (2017) for Si and the mean corrections of Mashonkina et al. (2011) and Bergemann et al. (2012b) for Fe I.

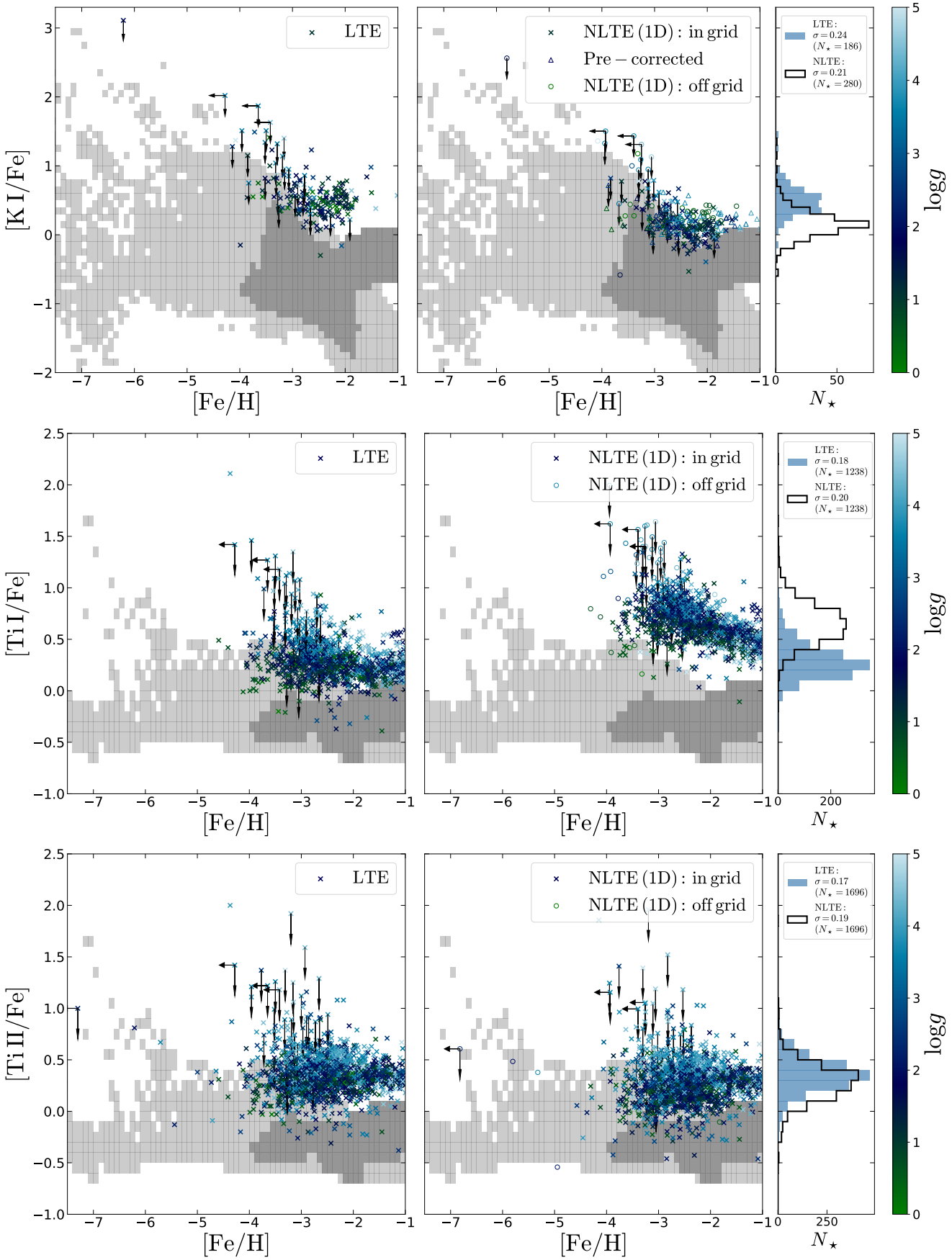

Fig. D.3: Same as Fig. 22 for [K/Fe] (top), [Ti I/Fe] (middle) and [Ti II/Fe] (bottom). Observed abundances have been corrected using the grids from Reggiani et al. (2019) for K, Bergemann (2011) for Ti I and Ti II, and the mean corrections of Mashonkina et al. (2011) and Bergemann et al. (2012b) for Fe I.

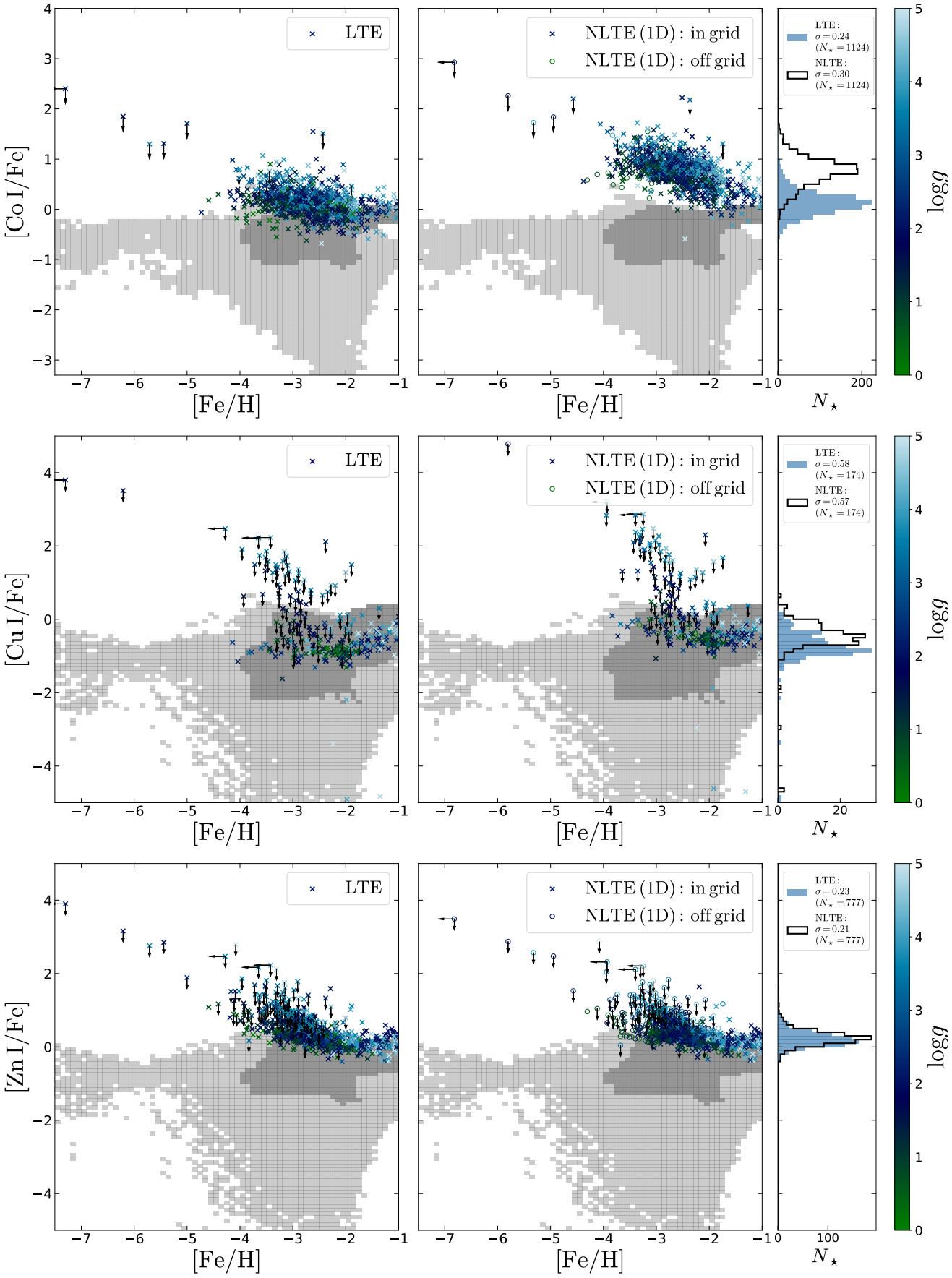

Fig. D.4: Same as Fig. 22 for [Co/Fe] (top), [Cu/Fe] (middle) and [Zn/Fe] (bottom). Observed abundances have been corrected using the grid from Bergemann et al. (2010) for Co I, the linear least-squares fit to the corrections of Shi et al. (2018), Andrievsky et al. (2018) and Xu et al. (2022) for Cu (see Sec. 3.21), the corrections of Sitnova et al. (2022) for Zn I and the mean corrections of Mashonkina et al. (2011) and Bergemann et al. (2012b) for Fe I.